crystals

MDPI

Article

Machine Learning-Based Predictions of Power Factor for Half-Heusler Phases

Kaja Bilińska and Maciej J. Winiarski *

Institute of Low Temperature and Structure Research, Polish Academy of Sciences, Okólna 2, 50-370 Wrocław, Poland
* Correspondence: m.winiarski@intibs.pl

Abstract: A support vector regression model for predictions of the thermoelectric power factor of half-Heusler phases was implemented based on elemental features of ions. The training subset was composed of 53 hH phases with 18 valence electrons. The target values were calculated within the density functional theory and Boltzmann equation. The best predictors out of over 2000 combinations regarded for the *p*-type power factor at room temperature are: electronegativity, the first ionization energy, and the valence electron count of constituent ions. The final results of support vector regression for 70 hH phases are compared with data available in the literature, revealing good ability to determine favorable thermoelectric materials, i.e., VRhGe, TaRhGe, VRuSb, NbRuAs, NbRuBi, LuNiAs, LuNiBi, TaFeBi, YNiAs, YNiBi, TaRuSb and NbFeSb. The results and discussion presented in this work should encourage further fusion of ab initio investigations and machine learning support, in which the elemental features of ions may be a sufficient input for reasonable predictions of intermetallics with promising thermoelectric performance.

Keywords: half-Heusler alloys; thermoelectric materials; machine learning; Support Vector Regression

Citation: Bilińska, K.; Winiarski, M.J. Machine Learning-Based Predictions of Power Factor for Half-Heusler Phases. *Crystals* **2024**, *14*, 354. https://doi.org/10.3390/cryst14040354

Academic Editor: Hongbin Bei

Received: 22 March 2024
Revised: 5 April 2024
Accepted: 8 April 2024
Published: 9 April 2024

1. Introduction

Machine Learning (ML) models are increasingly used as support for ab initio calculations of various properties of half-Heusler (hH) alloys [1–3]. Depending on the relations and character of the parameters investigated, different ML methods are employed, e.g., Boosted Decision Tree Regression, Multiple Linear Regression [2], or Random Forest Regression [1]. Recently, numerous targets were studied: stability [4], atomic site occupancy [5], lattice parameters [6], lattice thermal conductivity [7,8], characteristic features of band structures and band gaps [9,10], as well as spin polarization [11].

Careful investigations among 2000 combinations of eleven elemental properties of ions present in ternary hH compounds (up to 33-dimensional feature space) as potential predictors of structural and electronic properties for arbitrarily chosen subsets of hH systems (47 hH phases as the train-test records and 74 hH systems for predictions) were presented in the recent study [3]. The root mean squared errors of ML-based predictions for the lattice parameters (0.1 Å), bulk modulus (11–12 GPa), band gap (0.22 eV), and the lattice thermal conductivity (9–9.5 W/mK) proved general ability of the Support Vector Regression (SVR) methods to predict various properties of hH materials. The satisfactory performance of ML calculations encourage further studies on physical quantities, which are difficult to be obtained due to high computational cost, i.e., the examination of transport properties.

Thermoelectric (TE) performance of hH compounds draws wide interest due to very high values of the Power Factor (PF) reported for NbFeSb [12]. Theoretical investigations shown that the TE properties of this system may be successfully estimated based on the semi-classical transport coefficients [13]. The recent study indicated that novel As-based hH compounds (TaFeAs, VFeAs, and TiRuAs) may be thermodynamically stable and potentially valuable TE materials [14]. In spite of the fact that the number of stable hH

compounds is limited, the search for novel compositions with potential for TE applications remains an interesting field for further theoretical investigations.

The aim of the present work is to investigate PF of cubic XYZ hH phases that follow the 18 valence electron rule. The X and Y are transition metal ions, whereas Z is a main group element. First, the electronic structures of numerous novel hH systems are obtained with the DFT methods and discussed in detail. Next, the semi-classical transport coefficients of these phases are calculated. Finally, the values of PF for a large set of hH materials are estimated with the ML methods. The elemental features of X, Y, and Z ions are considered as predictors for ML models. The ability of SVR-based methods to determine hH systems that are favorable in terms of potential TE applications is discussed. The findings presented in this work may encourage further experimental efforts in synthesis of novel families of hH intermetallics.

2. Computational Details

The feature space for ML-support considered in this work encompasses properties of 53 hH phases with 18 valence electrons. The systems selected are expected to be stable according to the zero hull distance E_{HD} or likely stable ($E_{HD} \leq 0.1$ eV) [15–17]. The electronic structure calculations were performed with the use of the VASP package [18–21]. The fully relativistic mode was employed due to the strong spin–orbit coupling in hH systems. The cut-off energy of the plane–wave basis was set to 500 eV. The Exchange-Correlation (XC) functionals employed were Perdew-Burke-Ernzerhof [22] (GGA) and modified Becke–Johnson [23] (MBJGGA). The relaxation time of carriers, required for calculations of electrical conductivity, was obtained with the use of the Deformation Potential (DP) theory [24]. The lattice thermal conductivity was approximated following the Slack's formula [25]. The transport properties were calculated with the Boltzmann transport equation (BoltzTraP2 [26]). The $50 \times 50 \times 50$**k**-point mesh was used for this task.

The method of ML predictions was SVR [27] implemented in the sklearn library [28]. The gaussian radial basis kernel function was applied [29,30]. The essence of the SVR approach is a selection of a hyperplane in the multidimensional feature space that maximizes the number of points that fall within the decision boundary line [31]. SVR parameters, C (connected to the trade-off between the fitting the training data and the regularization), and γ (responsible for the flexibility of the model), were determined as follows: $C = 1$, $\gamma = (n * X_{VAR})^{-1}$, where X_{VAR} is a variation among the predictors and n is a number of features. Furthermore, the standard scaler as the train-test feature scaling was implemented. The cross-validation applied to the SVR models was the Leave One Out (LOO) approach [32]. The accuracy measure for the SVR model examination was the root mean square error (RMSE = $\sqrt{\frac{1}{n}\sum_{i=1}^{n}(a_i^{calc} - a_i^{pred})^2}$, where a is a quantity considered). The feature space of elemental properties for predictors was based on data taken from the WebElements periodic table (University of Sheffield [33]).

3. Results

The set of compounds considered in this work was created out of 34 novel stable hH systems [14], four already investigated Sb-bearing phases (YNiSb, YPdSb, LuNiSb, LuPdSb) [34], and additional 15 hH phases with the hull distance smaller or equal to 0.1 eV (according to the open quantum materials database [15,16]). Such a range of hull distance indicates stable or likely stable materials [17]. The theoretical estimations of formation energies for particular phases may be inaccurate and real systems often adopt metastable phases with values of the total energy above the hull curve. The resulting set of hH phases contains various transition metal ions at the atomic positions X and Y, as well as numerous Z ions from the p-block of the periodic table of elements. The large set of materials selected at this stage is expected to be a reasonable starting point for creation of feature spaces for SVR-models. Some well-known phases are included (mainly antimonides) in order to examine the performance of DFT calculations and SVR modelling with respect to the available literature data for hH alloys.

The selected properties of the 15 novel and additional Sb-bearing phases are listed in Table 1. The lattice parameters (from 5.796 Å for VRhGe up to 6.608 Å for YPdSb) and bulk modulus (from 88.15 GPa for YPdSb up to 185.13 GPa for TaRhGe) were obtained within the GGA approach. The band gaps E_{XC}, effective mass m for the hole- and electron-like carriers were obtained with the GGA and MBJGGA XC functionals. The novel hH systems are expected to exhibit narrow band gaps (smaller than 1.0 eV, except ZrCoAs, ZrRhAs and TaRhGe). Materials with E_g below 0.5 eV are generally desirable for TE performance at room temperature (e.g., E_g of 0.51 eV was reported for NbFeSb [13]). However, the systems with slightly bigger band gaps may also exhibit enhanced TE properties (e.g., TaFeSb with E_g of 0.81 eV [14]). In some cases, a strong disproportion between the electron and hole effective mass is found, which may favor one carrier regime in terms of the potential TE performance due to relatively long relaxation time of carriers, e.g., the *n*-type carriers in NbRuAs, VRuSb, and TaRhGe. Furthermore, some systems exhibit small m_h and m_e (e.g., HfRhAs and NbRuAs). Extremely low values of m_e (below 0.16) are predicted for NbRuAs, NbRuBi, TaRhGe with both XC functionals.

Table 1. Selected properties of 15 novel hH systems and (Y;Lu)(Ni;Pd)Sb: lattice parameter *a* (Å), bulk modulus *B* (GPa), GGA-derived band gap E_{GGA}, MBJGGA-derived band gap E_{MBJ} (eV), effective mass of electrons m^n and hole-like carriers m^p obtained with the GGA and MBJGGA functionals.

Comp.	*a*	*B*	E_{GGA}	E_{MBJ}	m^p_{GGA}	m^n_{GGA}	m^p_{MBJ}	m^n_{MBJ}
TiPdPb	6.328	103.88	0.352	0.324	0.65	0.70	0.66	0.64
TiPdGe	5.964	131.38	0.619	0.584	0.61	0.57	0.61	0.57
VRhGe	5.796	172.54	0.433	0.748	1.20	0.21	1.10	0.24
ZrCoAs	5.831	147.58	1.203	1.229	1.02	3.49	1.05	3.31
ZrRhAs	6.110	143.97	1.117	1.292	0.36	0.98	0.30	1.70
HfPdGe	6.142	133.71	0.552	0.506	0.40	0.61	0.31	0.61
HfRhAs	6.063	160.02	0.282	0.816	0.43	0.29	0.28	0.32
TaRhGe	5.973	185.13	1.044	1.026	0.79	0.14	0.83	0.15
VRuSb	6.044	165.64	0.189	0.631	0.53	0.19	0.52	0.23
ZrNiGe	5.893	141.57	0.679	0.654	0.83	0.71	0.60	0.74
ScPdAs	6.099	111.31	0.432	0.451	0.35	3.17	0.20	4.23
NbRuAs	5.961	183.13	0.337	0.506	0.36	0.11	0.37	0.12
TiNiPb	6.038	115.66	0.341	0.292	0.66	0.42	0.67	0.41
NbRuBi	6.307	151.77	0.383	0.557	0.42	0.13	0.52	0.16
LuNiAs	5.989	106.94	0.409	0.475	0.20	4.03	0.18	3.06
YNiSb	6.350	93.02	0.270	0.283	0.26	2.63	0.22	4.16
YPdSb	6.608	88.15	0.147	0.160	0.17	5.06	0.14	4.94
LuNiSb	6.269	97.16	0.207	0.193	0.21	2.70	0.18	3.56
LuPdSb	6.544	89.30	0.106	0.103	0.25	6.17	0.16	4.56

The lattice parameters obtained here for the (Y;Lu)(Ni;Pd)Sb phases are in good accordance with the literature data calculated within the full potential approach [34]. Similar comparisons for band gaps lead to relatively small discrepancies of 10–30 meV. The biggest one was found in the case of YPdSb, for which the reported previously E_{GGA} of 0.230 eV and E_{MBJ} of 0.198 eV [34] are clearly bigger than the values presented here: E_{GGA} of 0.147 eV and E_{MBJ} of 0.165 eV. Considering the bulk modulus, the discrepancy between the obtained here and literature results is complicated. The values of bulk modulus presented here for YNiSb and LuPdSb are close to the literature data [34,35], whereas the clear discrepancy is found for YPdSB and LuNiSb. It may be connected with the different ab initio software used (pseudopotential vs. full potential approach) and the fact that the high accuracy of the second derivative of the total energy is very difficult to be obtained. The values of the effective masses for Sb-bearing systems are close to those previously reported up to 0.05, 0.06, and 0.07 m_e (depending on the XC functional used) for YNiSb, YPdSb, and LuNiSb, respectively.

The band structures calculated for the 15 novel hH phases are presented in Figure 1. It is worth recalling that the spin-orbit coupling is a crucial factor for reasonable description of electronic structure of narrow band gap hH systems [34]. Although the effect of SOC is noticeable in valence band splittings of Ru-, Rh-, and Pd-bearing phases in Figure 1, it is relatively weak when compared to those reported for hH antimonides with lanthanide X ions. The materials studied here exhibit semiconducting character with the dominant indirect transition type, except HfRhAs and ZrRhAs with the direct Γ–Γ one (GGA). The band structures of NbRuAs and LuNiAs are similar to those of NbFeSb [12,13] and LuNiBi [36], respectively. ScPdAs and LuNiAs exhibit the specific shape of the conduction bands, with Conduction Band Minumum (CBM) located at the X point (from the MBJ approach for ScPdAs) or in between the X and Γ points (LuNiAs from GGA/MBJGGA and GGA-derived results for ScPdAs). The modifications in Valence Band Maximum (VBM) or CBM locations obtained with different XC functionals are observed in some cases, but not as commonly as the underestimation of E_{GGA} with respect to E_{MBJ}. It is a well-known fact that the modified Becke-Johnson potential is dedicated to studies on semiconductors. Despite that MBJGGA-derived results may be assumed to be more realistic than the GGA ones [23], hH alloys are complex intermetallics and final examinations of theoretical predictions of their electronic structures should be based on further experimental investigations.

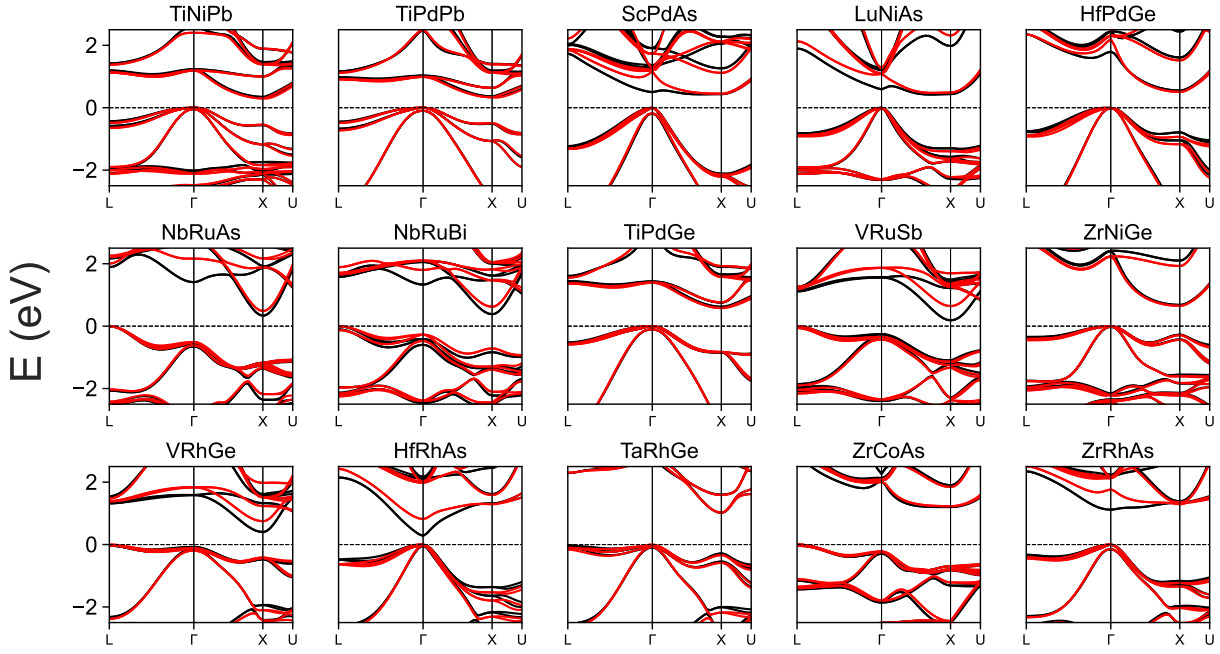

Figure 1. Bandstructures of hH alloys with hull distance ranged from 0 eV < E_{HD} ≤ 0.1 eV. The results of GGA and MBJGGA are marked with black and red lines, respectively.

One may find some general similarities between the positions and shapes of VBM and CBM in compounds with similar composition (e.g., TiNiPb, TiPdPb, and TiPdGe). The widening of E_g due to the relatively light ion Z is observed between TiPdPb and TiPdGe from both XC functionals applied. However, the opposite effect is present in NbRuAs and NbRuBi, which is related to a relatively big volume of a unit cell of the Bi-based phase. The widening of E_g connected with the relatively heavier Y ion is also found in TiNiPb and TiPdPb. Furthermore, the differences between the band structures of ZrCoAs and ZrRhAs are substantial in terms of the shift in positions of VBM and CBM.

Based on the commonly held belief that heavy carriers result in good TE performance due to high Seebeck coefficient, one shall desire possibly flat valence bands in the vicinity of VBM (the p-type regime) or in the vicinity of CBM (the n-type regime). However, Pei et al. [37] questioned this statement, providing examples of good TE hH materials with low effective mass (inferred from the steep bands in the vicinity of VBM or CBM). The

low values of effective mass were also reported for hH antimonides [34]. They lead to very long relaxation times, which is desirable for TE performance. According to the results for *n*- or *p*-type carries, gathered in Table 1, some systems considered in this work may exhibit exceptional relaxation times (e.g., the Ru-bearing phases in the *n*-type regime). The presence of additional valence bands below VBM in arsenides and germanides may indicate high values of Seebeck coefficient in the *p*-type channel in these systems. Some germanides, i.e., VRhGe and TaRhGe, may exhibit the almost degenerate VBM at the *L* and Γ points.

The TE PF at room temperature for the novel hH systems, based on the results of transport calculations, is presented in Figure 2. The majority of hH phases considered here are expected to exhibit PF lower than 2 mW/K^{2}m, regardless of the applied XCF. The highest values of PF are found for the *n*-type carriers. In particular, the greatest PF of over 4 mW/K^{2}m was obtained (GGA) for NbRuAs. Similarly, VRuSb, TaRhGe, VRhGe, LuNiAs and LuNiSb (in order corresponding to decreasing PF) emerge as promising candidates on TE systems in the *n*- or *p*-type regimes. It is worth noting that the optimal carrier concentrations (10^{18}–10^{20}) are rather feasible to be obtained in real materials.

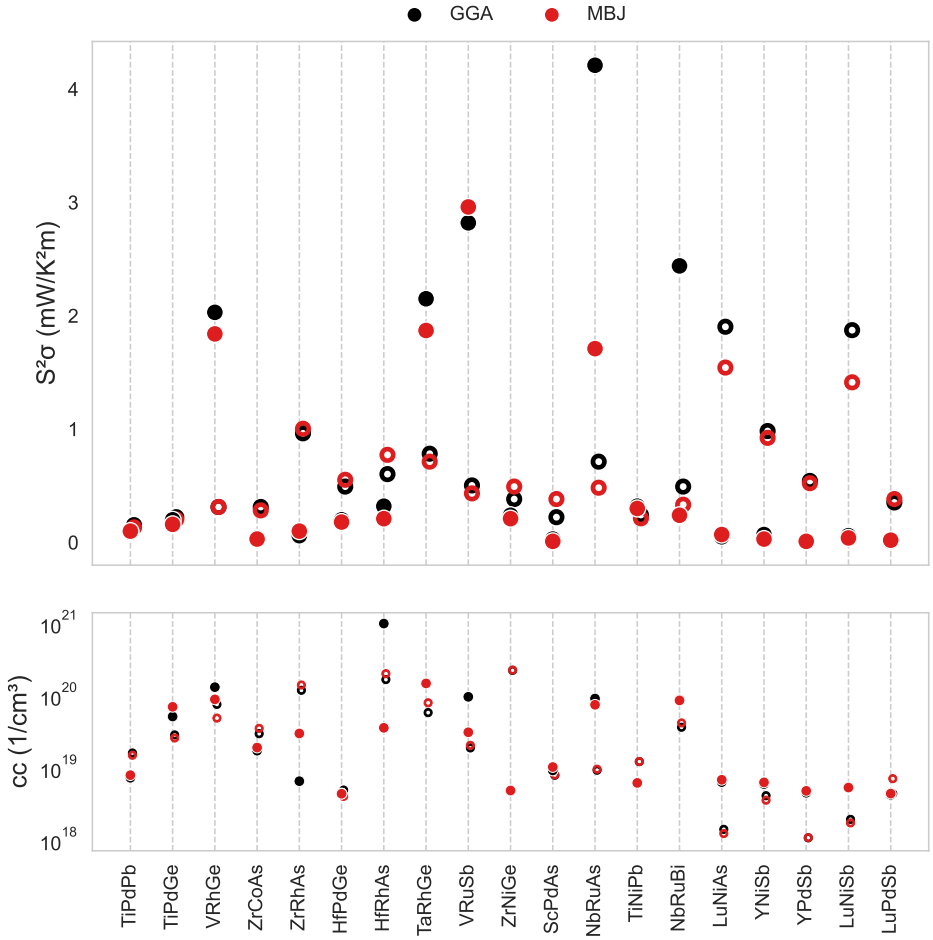

Figure 2. Maximal PF at room temperature for 15 novel hH systems and (Y;Lu)(Ni;Pd)Sb. The results of GGA and MBJGGA are marked with black and red colors. Different point types indicate electrons (full dots for the *n*-type regime) and holes (circles for the *p*-type regime). The respective values of carrier concentration are given in the bottom plot.

Some electronic properties of the 15 novel compounds were already discussed in the literature, e.g., the band gap of TiPdPb in terms of potential TE applications [38] and its lattice thermal conductivity (theoretical analysis) [7,8]. The DFT (GGA) study by Kalita et al. [39] on TiPdPb resulted in a relatively low value of the lattice thermal conductivity (0.98 W/mK) and a figure of merit (ZT) of 0.64 at 1000 K in the *p*-type regime.

Similar value of ZT was obtained for TiPdGe, but at high temperature [39]. However, PF^{p}_{GGA} of these systems was not explicitly discussed. The Ge-bearing phases, VRhGe and HfPdGe, were also analyzed in terms of TE performance at high temperature [40,41]. Considering antimonides, Kaur et al. reported VRuSb as the favourable TE material [42]. NbRuAs is the only system among the As-bearing hH alloys, which was investigated in terms of the potential TE application. Cherifi et al. [43] predicted ZT of 0.30 at room temperature and 0.62 at 1000 K for this compound in the *p*-type regime. The relatively high PF in NbRuAs is also reflected in the results presented here. The lack of any data for other As-bearing phases (ZrCoAs, ZrRhAs, HfRhAs, ScPdAs, and LuNiAs) may encourage further studies on this family of compounds. Also, there is a lack of literature reports on TE performance of TiNiPb and NbRuBi [8,44]. The comprehensive theoretical results (GGA and MBJGGA) were only reported for antimonides: YNiSb, YPdSb, LuNiSb, and LuPdSb [34]. The PF values obtained here with the pseudopotenial approach are significantly lower. However, the dominant character of the *p*-type regime is clearly noticeable and the promising TE performance of LuNiSb and YNiSb is confirmed. The origin of a relatively big discrepancy in PF between the present results and literature data for antimonides is connected with a complex scheme of calculations of the relaxation time of carriers. Namely, a small variation in the deformation potential may lead to a significant reduction or extension in relaxation time for a particular compound.

As the predictors for SVR models, the following features of the elements in the *XYZ* phases were employed: atomic mass `u`, atomic radius `r`, molar volume `V`, density of a solid `g`, electronegativity `n`, Debye temperature `T`, thermal conductivity `k`, I–III ionization energies: `i(I)`, `i(II)`, `i(III)`, and Valence Electron Count `VEC`. According to the previous ML studies [2,3,7,8], these features were found to be relevant for modelling of various properties of hH phases. The targets examined based on the listed predictors were PF and ZT at 300 K in the *p* and *n*-regimes. All possible combinations of the predictors (starting with a single predictor up to the feature space constructed out of eleven elemental features for each ion in *XYZ*) were examined for each target. The SVR model predicting PF (GGA) for the *p*-type carriers at room temperature was found to be the best among the set considered and the properties and results of this model are further discussed. It is worth recalling that an estimation of PF for a material may be more desirable for discussion of TE performance of real devices than a search for high ZT [45].

As depicted in Figure 3a, the lowest values of RMSE are achieved for feature sets with limited cardinality. The biggest RMSE values were obtained for single-predictor feature spaces (i.e., `i(III)`), whereas the optimal RMSE was revealed for more than one dominant combination. Neither the most nor the least numerous combinations of predictors minimize RMSE for the particular model, which justifies the requirement of testing of various combinations of predictors. Analogous observations were reported for SVR models for different physical properties of hH systems [3]. Nevertheless, the general hint on the crucial elemental factors for the target may be the fact that over 150 favourable combinations (from RMSE of 0.319 mW/K^{2}m for `[n, r, k, i(I), VEC]` and `[n, i(I), VEC]` to RMSE of 0.339 mW/K^{2}m for `[g, k, i(III), VEC]`) included at least one of the following predictors: `n`, `i(I)`, and `VEC`. The significance of the indicated properties is in accord with the favourable features found in SVR modelling of other parameters of hH phases [3], i.e., i(I) and VEC were crucial for band gaps. Whereas `n` and `i(I)` may reflect the width of a band gap and the effective mass, `VEC` may be connected with some characteristic features of band structures, e.g., the number and shape of valence bands. The predictive power of SVR model based on such a simple combination of three fundamental properties of elements is particularly interesting due to the fact that TE performance is a complex phenomenon.

The examples of learning curves for LOO cross-validation for the favourable three combinations of predictors (`[n, r, k, i(I), VEC]`, `[n, k, i(I), VEC]`, `[n, i(I), VEC]` are depicted in Figure 3b. One can notice the relatively high initial RMSE for the least numerous train subsets: $RMSE_{n=25}$ = 0.438, 0.433, and 0.447 mW/K^{2}m for `[n, r, k, i(I), VEC]`, `[n, k, i(I), VEC]`, and `[n, i(I), VEC]`, respectively. There is a clear decrease in

RMSE with the increasing size of the training subsets and the final values of RMSE are significantly lower ($RMSE_{n=50}$ = 0.324, 0.326, and 0.308 mW/K^{2}m for `[n, r, k, i(I), VEC]`, `[n, k, i(I), VEC]`, and `[n, i(I), VEC]`, respectively). Although no clear plateau was reached, the range of PF targets in the training set is relatively wide and the RMSE value of ≈0.3 mW/K^{2}m may be considered as satisfactory. It is also worth noting that the number of stable hH materials limits the training data and the set of compounds for final predictions.

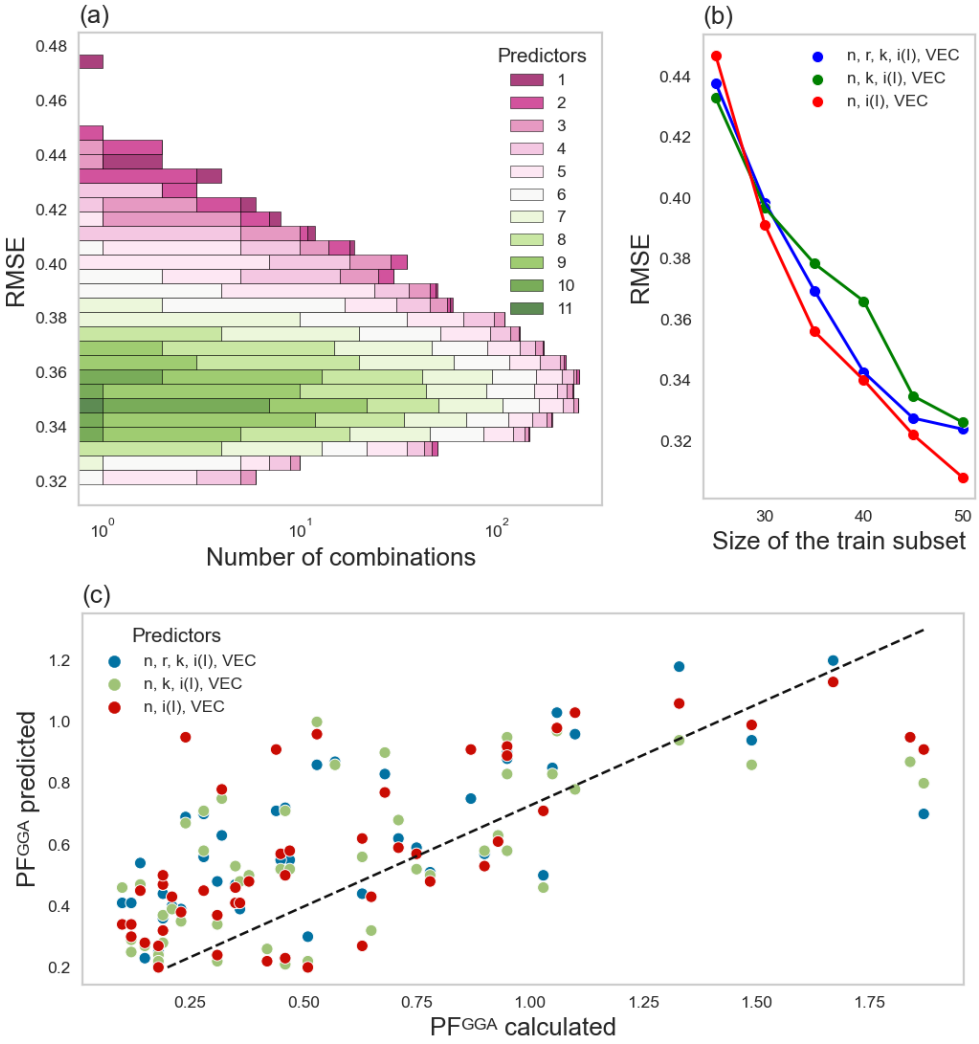

Figure 3. Parameters and results of the SVR model. In (**a**), the distribution of over 2000 combinations of the elemental predictors (from a single element to all eleven predictors included) as the function of the RMSE for PF^{p}_{GGA} (mW/K^{2}m) predictions. In (**b**), the learning curves for `[n, r, k, i(I), VEC]` (blue), `[n, k, i(I), VEC]` (green), and `[n, i(I), VEC]` (red). In (**c**), the validation with the use of DFT and SVR-derived values of PF for GGA parametrization for three combinations of predictors: `[n, r, k, i(I), VEC]` (blue), `[n, k, i(I), VEC]` (green), and `[n, i(I), VEC]` (red).

Figure 3c displays the validation of PF^{p}_{GGA} (DFT-derived vs. SVR-based results) for the optimal sets of predictors. The SVR models yield the average of the predicted values based on the $n-1$ repetitions of modeling with the use of the LOO approach. The `[n, i(I), VEC]` set is the most favourable, because it minimize not only RMSE, but also the number of predictors required. The distributions shown in Figure 3c indicate a general consistency between models compared. A clear (but not exactly linear) trend between the SVR-derived predictions and DFT-based results is noticeable in all cases. The range of predicted target values is reduced when compared with that of the train-

ing data. The predictions of PF^{p}_{GGA} for the majority of systems fall within the RMSE range for the best combinations of predictors (i.e., 0.319 mW/K^{2}m for `[n, r, k, i(I), VEC]` and `[n, i(I), VEC]`; 0.321 mW/K^{2}m for `[n, k, i(I), VEC]`). As one may expect, the greatest discrepancies ΔPF^{p}_{GGA} between the DFT- and SVR-derived values (for predictors `[n, i(I), VEC]`) were observed in the cases of the highest PF^{p}_{GGA}, e.g., for LuNiAs (PF^{p}_{GGA} calculated = 1.87 mW/K^{2}m, ΔPF^{p}_{GGA} = 0.96 mW/K^{2}m) and LuNiSb (PF^{p}_{GGA} calculated = 1.84 mW/K^{2}m, ΔPF^{p}_{GGA} = 0.89 mW/K^{2}m). This finding is a direct consequence of the poor ability of any ML model to predict values that strongly deviate and are sparse due to the lack of sufficient data available [27]. One may consider SVR-based estimations as a rather qualitative results, which may be useful in a large scale search for novel materials. Systems selected within this approach should be further investigated with exact theoretical methods or in experimental studies.

The results of final SVR predictions of PF^{p}_{GGA} based on `[n, i(I), VEC]` feature space are gathered in Table 2. The range of PF^{p}_{GGA} is from 0.16 mW/K^{2}m (ScPdSb) to 1.11 mW/K^{2}m (LuNiBi). The median and mean values for 70 hH systems are almost equal (0.47 and 0.48 mW/K^2, respectively). One of the most comprehensively investigated hH phases is NbFeSb with remarkably high PF and ZT from both experimental and theoretical reports on various temperature ranges [12,13]. The value of PF^{p}_{GGA} obtained for this compound with SVR is smaller than those reported in the literature, but NbFeSb is still one of the most promising hH phases (PF^{p}_{GGA} of 0.83 mW/K^{2}m). Similar discussion was already presented for high-PF systems in the training set (LuNiAs and LuNiSb). The highest PF was predicted for LuNiBi, which was recently reported to exhibit relatively high PF at room temperature in the *p*-type regime [36,46]. Another hH phases with high TE performance predicted here are: TaFeBi, YNiAs, YNiBi, TaRuSb, TaRuBi, TaOsSb, VOsAs, NbOsAs, VRuAs and ScNiAs. According to the literature data, TaFeBi [47], TaOsSb [48], YNiBi (ZT up to 0.12 [49]), TaRuSb (PF over 10 mWm/K^2 [50]), VRuAs (PF up to 185.37 W/msK^2 at 1000 K [51]), and ScNiAs [52,53] were already considered as high-PF hH phases. However, some promising TE candidate compounds were predicted here to exhibit low PF, e.g., ScPtSb [35]. Some phases may also adopt different crystal structures, e.g., YNiAs may prefer the hexagonal $P63/mmc$ phase according to the formation energies [15,16].

Table 2. SVR-derived values of PF^{p}_{GGA} (mW/K^{2}m) at 300 K based on the `[n, i(I), VEC]` predictors.

Compd	PF^{p}_{GGA}	Compd	PF^{p}_{GGA}	Compd	PF^{p}_{GGA}	Compd	PF^{p}_{GGA}	Compd	PF^{p}_{GGA}
HfNiGe	0.40	NbIrPb	0.29	TaIrSn	0.53	VCoSn	0.68	YPdAs	0.30
HfRhBi	0.47	NbCoSn	0.69	TaIrPb	0.35	VRhSn	0.26	YPtSb	0.37
HfNiPb	0.31	NbCoPb	0.34	TaRuSb	0.84	VIrSn	0.41	ZrNiSn	0.34
HfRhSb	0.55	NbOsSb	0.60	TaRuBi	0.77	VRuAs	0.72	ZrNiPb	0.30
HfPdPb	0.19	NbFeSb	0.83	TaOsSb	0.77	VOsSb	0.61	ZrPdGe	0.22
HfPtSn	0.24	NbFeBi	0.70	TaCoPb	0.41	VRuBi	0.49	ZrPdPb	0.18
HfPtPb	0.18	ScNiAs	0.72	TaFeBi	1.10	VOsAs	0.73	ZrPtSn	0.23
HfCoSb	0.51	ScNiSb	0.64	TiNiSn	0.28	VOsBi	0.53	ZrCoSb	0.51
LuNiBi	1.11	ScNiBi	0.59	TiPdSn	0.19	VCoPb	0.35	ZrCoBi	0.52
NbRhGe	0.34	ScPdSb	0.16	TiPtPb	0.18	VRhPb	0.38	ZrRhSb	0.56
NbOsAs	0.72	ScPtSb	0.28	TiCoSb	0.65	VIrPb	0.30	ZrRhBi	0.47
NbOsBi	0.53	TaRhSn	0.64	TiRhSb	0.52	VFeBi	0.68	ZrIrAs	0.31
NbRhSn	0.27	TaRhPb	0.43	TiIrAs	0.54	YNiAs	0.90	ZrIrSb	0.25
NbRhPb	0.37	TaIrGe	0.58	TiIrBi	0.35	YNiBi	0.85	ZrIrBi	0.22

The TE properties of YNiAs, NbOsAs, TaRuBi, and VOsAs were not studied up to now. The TE performance of hH arsenides seems to be an interesting direction for further investigations. The findings based on SVR modeling are consistent with the characteristic features of electronic structure of As-based hH compounds, which were discussed in detail for NbRuAs (low effective mass and numerous valence bands). The recent interest

in As-bearing hH phases [38,51,54–57] supports this suggestion and encourage further experimental efforts in synthesis of such materials.

4. Conclusions

DFT calculations for novel hH phases revealed comprehensive insight into their electronic structure and TE performance in the *p* and *n*-type regimes for two XC functionals (GGA and MBJGGA). High values of *n*-type PF calculated for VRhGe, TaRhGe, VRuSb, and NbRuAs indicate these systems as new promising TE compounds. Their superior transport properties are directly connected with characteristic features of band structures, i.e., low effective mass of carries and numerous bands in the vicinity of CBM.

Further SVR modelling of *p*-type regime PF_{GGA} (found the best due to the RMSE and validation), based on elemental features of *XYZ* ions (electronegativity, the first ionization energy, valence electron count), also revealed predictive power for novel TE materials. Numerous phases: ZrCoAs, ZrRhAs, HfRhAs, ScPdAs, LuNiAs, and NbRuBi are expected to be interesting subjects for extended theoretical and experimental studies. Despite some limitations, the combined DFT- and ML-based investigations may accelerate the development in computational materials science.

Author Contributions: K.B.: Methodology, Investigation, Visualization, Writing. M.J.W.: Conceptualization, Methodology, Resources, Writing, Supervision. All authors have read and agreed to the published version of the manuscript.

Funding: Calculations for this work were performed at Wroclaw Center for Networking and Supercomputing (Project No. 158).

Data Availability Statement: The datasets generated during and/or analyzed during the current study are available from the corresponding author on reasonable request.

Conflicts of Interest: The authors declare that they have no known competing financial interests or personal relationships that could have appeared to influence the work reported in this paper.

References

1. Carrete, J.; Li, W.; Mingo, N.; Wang, S.; Curtarolo, S. Finding unprecedentedly low-thermal-conductivity half-Heusler semiconductors via high-throughput materials modeling. *Phys. Rev. X* **2014**, *4*, 011019. [CrossRef]
2. Miyazaki, H.; Tamura, T.; Mikami, M.; Watanabe, K.; Ide, N.; Ozkendir, O.M.; Nishino, Y. Machine learning based prediction of lattice thermal conductivity for half-Heusler compounds using atomic information. *Sci. Rep.* **2021**, *11*, 13410. [CrossRef] [PubMed]
3. Bilińska, K.; Winiarski, M.J. Machine Learning-Based Predictions for Half-Heusler Phases. *Inorganics* **2024**, *12*, 5. [CrossRef]
4. Gautier, R.; Zhang, X.; Hu, L.; Yu, L.; Lin, Y.; Sunde, T.O.; Chon, D.; Paeppelmeirer, K.; Zunger, A. Prediction and accelerated laboratory discovery of previously unknown 18-electron ABX compounds. *Nat. Chem.* **2015**, *7*, 308–316. [CrossRef] [PubMed]
5. Gzyl, A.S.; Oliynyk, A.O.; Adutwum, L.A.; Mar, A. Solving the Coloring Problem in Half-Heusler Structures: Machine-Learning Predictions and Experimental Validation. *Inorg. Chem.* **2019**, *58*, 9280–9289. [CrossRef] [PubMed]
6. Zhang, Y.; Xu, X. Machine learning modeling of lattice constants for half-Heusler alloys. *AIP Adv.* **2020**, *10*, 045121. [CrossRef]
7. Tranås, R.; Løvvik, O. M.; Tomic, O.; Berland, K. Lattice thermal conductivity of half-Heuslers with density functional theory and machine learning: Enhancing predictivity by active sampling with principal component analysis. *Comput. Mater. Sci.* **2022**, *202*, 110938. [CrossRef]
8. Tranås, R.; Løvvik, O.M.; Berland, K. Lattice Thermal Conductivity from First Principles and Active Learning with Gaussian Process Regression. *arXiv* **2023**, arXiv:2309.06786.
9. Dylla, M.T.; Dunn, A.; An, S.; Jain, A.; Snyder, G.J. Machine learning chemical guidelines for engineering electronic structures in half-heusler thermoelectric materials. *Research* **2020**, *2020* , 6375171. [CrossRef] [PubMed]
10. Choudhary, M.K.; Raj V.A.; Ravindran, P. Composition and Structure Based GGA Bandgap Prediction Using Machine Learning Approach. *arXiv* **2023**, arXiv:2309.07424.
11. Kurniawan, I.; Miura, Y.; Hono, K. Machine learning study of highly spin-polarized Heusler alloys at finite temperature. *Phys. Rev. Mater.* **2022**, *6*, L091402. [CrossRef]
12. Fu, C.; Zhu, T.; Liu, Y.; Xie, H.; Zhao, X. Band engineering of high performance p-type FeNbSb based half-Heusler thermoelectric materials for figure of merit zT > 1. *Energy Environ. Sci.* **2015**, *8*, 216–220. [CrossRef]
13. Fang, T.; Zheng, S.; Chen, H.; Cheng, H.; Wang, L.; Zhang, P. Electronic structure and thermoelectric properties of p-type half-Heusler compound NbFeSb: A first-principles study. *RSC Adv.* **2016**, *6*, 10507–10512. [CrossRef]

14. Bilińska, K.; Winiarski, M.J. High-Throughput Exploration of Half-Heusler Phases for Thermoelectric Applications. *Crystals* **2023**, *13*, 1378. [CrossRef]
15. Saal, J.E.; Kirklin, S.; Aykol, M.; Meredig, B.; Wolverton, C. Materials Design and Discovery with High-Throughput Density Functional Theory: The Open Quantum Materials Database (OQMD). *JOM* **2013** *65*, 1501–1509. [CrossRef]
16. Kirklin, S.S.; Saal, J.E.; Meredig, B.; Thompson, A.; Doak, J.W.; Aykol, M.; Rühl, S.; Wolverton, C. The Open Quantum Materials Database (OQMD): Assessing the accuracy of DFT formation energies. *npj Comput. Mater.* **2015**, *1*, 15010. [CrossRef]
17. Aykol, M.; Dwaraknath, S.S.; Sun, W.; Persson, K.A. Thermodynamic limit for synthesis of metastable inorganic materials. *Sci. Adv.* **2018**, *4*, eaaq0148. [CrossRef]
18. Kresse, G.; Hafner, J. Ab initio molecular dynamics for open-shell transition metals. *Phys. Rev. B* **1993**, *48*, 13115. [CrossRef] [PubMed]
19. Kresse, G.; Hafner, J. Ab initio molecular-dynamics simulation of the liquid-metal–amorphous-semiconductor transition in germanium. *Phys. Rev. B* **1994**, *49*, 14251. [CrossRef]
20. Kresse, G.; Furthmüller, J. Efficiency of ab-initio total energy calculations for metals and semiconductors using a plane-wave basis set. *Comput. Mater. Sci.* **1996**, *6*, 15–50. [CrossRef]
21. Kresse, G.; Furthmüller, J. Efficient iterative schemes for ab initio total-energy calculations using a plane-wave basis set. *Phys. Rev. B* **1996**, *54*, 11169. [CrossRef] [PubMed]
22. Perdew, J.P.; Burke, K.; Ernzerhof, M. Generalized gradient approximation made simple. *Phys. Rev. Lett.* **1996**, *77*, 3865. [CrossRef]
23. Tran, F.; Blaha, P. Accurate band gaps of semiconductors and insulators with a semilocal exchange-correlation potential. *Phys. Rev. Lett.* **2009**, *102*, 226401. [CrossRef] [PubMed]
24. Bardeen, J.; Shockley, W.J.P.R. Deformation potentials and mobilities in non-polar crystals. *Phys. Rev.* **1950** *80*, 72 [CrossRef]
25. Slack, G.A. Nonmetallic crystals with high thermal conductivity. *J. Phys. Chem. Solids* **1973**, *34*, 321–335. [CrossRef]
26. Madsen, G.K.H.; Carrete, J.; Verstraete, M.J. BoltzTraP2, a program for interpolating band structures and calculating semi-classical transport coefficients. *Comput. Phys. Commun.* **2018**, *231*, 140–145. [CrossRef]
27. Smola, A.J.; Schölkopf, B. A tutorial on support vector regression. *Stat. Comput.* **2004**, *14*, 199–222. [CrossRef]
28. Pedregosa, F.; Varoquaux, G.; Gramfort, A.; Michel, V.; Thirion, B.; Grisel, O.; Blondel, M.; Prettenhofer, P.; Weiss, R.; Dubourg, V.V.; et al. Scikit-learn: Machine Learning in Python. *J. Mach. Learn. Res.* **2011**, *12*, 2825–2830.
29. Rohmah, M.F.; Putra, I.K.G.D.; Hartati, R.S.; Ardiantoro, L. Comparison four kernels of svr to predict consumer price index. *J. Phys. Conf. Ser.* **2021**, *1737*, 012018. [CrossRef]
30. Fornberg, B.; Larsson, E.; Flyer, N. Stable computations with Gaussian radial basis functions. *SIAM J. Sci. Comput.* **2011**, *33*, 869–892. [CrossRef]
31. Awad, M.; Khanna, R.; Awad, M.; Khanna, R. Support vector regression. In *Efficient Learning Machines: Theories, Concepts, and Applications for Engineers and System Designers*; Springer: Berlin/Heidelberg, Germany, 2015; pp. 67–80.
32. Elisseeff, A.; Pontil, M. Leave-one-out error and stability of learning algorithms with applications. *NATO Sci. Ser. III Comput. Syst. Sci.* **2003**, *190*, 111–130.
33. WebElements. Available online: https://www.webelements.com (accessed on 13 November 2023).
34. Winiarski, M.J.; Bilińska, K. High termoelectric power factors of p-type half-Heusler alloys YNiSb, LuNiSb, YPdSb, and LuPdSb. *Intermetallics* **2019**, *108*, 55–60. [CrossRef]
35. Winiarski, M.J.; Bilińska, K.; Kaczorowski, D.; Ciesielski, K. Thermoelectric performance of p-type half-Heusler alloys ScMSb (M = Ni, Pd, Pt) by ab initio calculation. *J. Alloys Compd.* **2018**, *762*, 901–905. [CrossRef]
36. Winiarskia, M.J.; Bilinska, K. Power Factors of p-type Half-Heusler Alloys ScNiBi, YNiBi, and LuNiBi by ab initio Calculations. *Acta Phys. Pol. A.* **2020**, *138*, 533–538. [CrossRef]
37. Pei, Y.; LaLonde, A.D.; Wang, H.; Snyder, G.J. Low effective mass leading to high thermoelectric performance. *Energy Environ. Sci.* **2012**, *5*, 7963–7969. [CrossRef]
38. Bilińska, K.; Winiarski, M.J. Search for semiconducting materials among 18-electron half-Heusler alloys. *Solid State Commun.* **2023**, *365*, 115133. [CrossRef]
39. Kalita, D.; Limbu, N.; Ram, M.; Saxena, A. DFT study of structural, mechanical, thermodynamic, electronic, and thermoelectric properties of new PdTi Z (Z= Ge and Pb) half Heusler compounds. *Int. J. Quantum Chem.* **2022**, *122*, e26951. [CrossRef]
40. Solola, G.T.; Bamgbose, M.K.; Adebambo, P.O.; Ayedun, F.; Adebayo, G.A. First-principles investigations of structural, electronic, vibrational, and thermoelectric properties of half-Heusler VYGe (Y= Rh, Co, Ir) compounds. *Comput. Condens. Matter* **2023**, *36*, e00827. [CrossRef]
41. Bendahma, F.; Mana, M.; Terkhi, S.; Cherid, S.; Bestani, B.; Bentata, S. Investigation of high figure of merit in semiconductor XHfGe (X= Ni and Pd) half-Heusler alloys: Ab-initio study. *Comput. Condens. Matter* **2019**, *21*, e00407. [CrossRef]
42. Kaur, K.; Kumar, R. On the possibility of thermoelectricity in half Heusler XRuSb (X= V, Nb, Ta) materials: A first principles prospective. *J. Phys. Chem. Solids* **2017**, *110*, 108–115. [CrossRef]
43. Cherifi, F.; Mostefa, Z.; Boukra, A.; Meghoufel, Z.F.; Bouattou, M.; Kadi Allah, F.; Terki, F. Thermoelectric Transport Parameters of p-Type RuVAs and RuNbAs Heusler Alloys. *Phys. Status Solidi B Basic Res.* **2020**, *257*, 2000271. [CrossRef]
44. Hong, D.; Zeng, W.; Xin, Z.; Liu, F.S.; Tang, B.; Liu, Q.J. First-principles calculations of structural, mechanical and electronic properties of TiNi-X (X= C, Si, Ge, Sn, Pb) alloys. *Int. J. Mod. Phys. B* **2019**, *33*, 1950167. [CrossRef]

45. Narducci, D. Do we really need high thermoelectric figures of merit? A critical appraisal to the power conversion efficiency of thermoelectric materials. *Appl. Phys. Lett.* **2011**, *99*, 102104. [CrossRef]
46. Touia, A.; Benyahia, K.; Tekin, A. First-principles calculations of structural, electronic, optical, and thermoelectric properties of LuNiBi and LuNiSb half-heusler. *J. Supercond. Nov. Magn.* **2021**, *34*, 2689–2698. [CrossRef]
47. Singh, S.; Zeeshan, M.; Brink, J.V.D.; Kandpal, H.C. Ab initio study of Bi-based half Heusler alloys as potential thermoelectric prospects. *arXiv* **2019**, arXiv:1904.02488.
48. Yazdani-Kachoei, M.; Li, S.; Sun, W.; Allaei, S.M.V.; Di Marco, I. Role of volume change on the physics of thermoelectric half-Heusler compounds. *Phys. Rev. Mater.* **2023**, *7*, 104602. [CrossRef]
49. Li, S.; Zhao, H.; Li, D.; Jin, S.; Gu, L. Synthesis and thermoelectric properties of half-Heusler alloy YNiBi. *J. Appl. Phys.* **2015**, *117*, 205101. [CrossRef]
50. Fang, T.; Zheng, S.; Zhou, T.; Yan, L.; Zhang, P. Computational prediction of high thermoelectric performance in p-type half-Heusler compounds with low band effective mass. *PCCP* **2017**, *19*, 4411–4417. [CrossRef]
51. Akinlami, J.O.; Odeyemi, O.O.; Omeike, M.O.; Adebayo, G.A. First principle calculations of the structural, elastic, electronic and transport properties of XRuAs (X = Ta and V). *Mater. Sci. Semicond.* **2022**, *148*, 106837. [CrossRef]
52. Jaishi, D.R.; Sharma, N.; Karki, B.; Belbase, B.P.; Adhikari, R.P.; Ghimire, M.P. Electronic structure and thermoelectric properties of half-Heusler alloys NiTZ. *AIP Adv.* **2021**, *11*, 025304. [CrossRef]
53. Mafe, A.S.; Shogo, O.E.; Bello, B.W.; Musari, A.A. Systematic study of stable palladium and nickel based half-Heusler compounds for thermoelectric generators. *Solid State Sci.* **2024**, *149*, 107451. [CrossRef]
54. Kaur, K.; Kumar, R. Ti based half Heusler compounds: A new on the screen with robustic thermoelectric performance. *J. Alloys Compd.* **2017**, *727*, 1171–1177. [CrossRef]
55. Benallou, Y.; Amara, K.; Doumi, B.; Arbouche, O.; Zemouli, M.; Bekki, B.; Mokaddem, A. Structural stability, electronic structure, and novel transport properties with high thermoelectric performances of ZrIrX (X = As, Bi, and Sb). *J. Comput. Electron.* **2017**, *16*, 1–11. [CrossRef]
56. Rani, B.; Khandy, S.A.; Singh, J.; Verma, A.S.; Ali, A.M.; Dhiman, S.; Kaur, K. Electronic structure, elastic and transport properties of new Palladium-based Half-Heusler Materials for Thermoelectric Applications. *Mater. Today Commun.* **2023**, *2023*, *106461*. [CrossRef]
57. Lazab, M.; Djebour, B.; Bouafia, H.; Bousmaha, M.; Sahli, B.; Boudia, K. Mechanical and dynamical stability, electronic and bonding properties of a new narrow-gap semiconductor YPdAs Half-Heusler: DFT and QTAIM study. *Mater. Sci. Semicond.* **2024**, *173*, 108160. [CrossRef]